

**Distilling two-atom distance information from intensity-intensity correlation functions**Jun-Tao Chang,<sup>1</sup> Jörg Evers,<sup>2,1</sup> and M. Suhail Zubairy<sup>1,\*</sup><sup>1</sup>*Institute for Quantum Studies and Department of Physics, Texas A&M University, College Station, Texas 77843, USA*<sup>2</sup>*Max-Planck-Institut für Kernphysik, Saupfercheckweg 1, D-69117 Heidelberg, Germany*

(Received 11 April 2006; published 31 October 2006)

The intensity-intensity correlation function of the resonance fluorescence light of two two-level atoms driven by a resonant standing-wave laser field is examined. Our aim is to gain information on the distance between the two atoms from observables accessible in experiments. For this, we numerically solve the time-evolution equations of the system and calculate the steady-state intensity-intensity correlation by using the Laplace transform and quantum regression theory. By varying the interatomic distance from about half a wavelength down to small fractions of a wavelength, we show that the correlation function exhibits characteristic properties for different distance ranges. Based on these results, we propose a scheme to obtain interatomic distance information from the power spectrum of the correlation function, which allows us to extract the desired distance information over a wide range of distances with high accuracy.

DOI: [10.1103/PhysRevA.74.043820](https://doi.org/10.1103/PhysRevA.74.043820)

PACS number(s): 42.50.Ct, 42.50.Ar

**I. INTRODUCTION**

Precise atomic position measurement has attracted a great deal of interest for many years. It has many applications such as atom lithography, microscopy, and atom imaging. However, due to the optical diffraction, in classical lens-based optical microscopy or imaging, the resolution in the focus plane cannot exceed the limit of half the wavelength of the illuminating light. In the past several decades, many methods have been developed to overcome this limit. Lens-based techniques include confocal [1], nonlinear femtosecond, and stimulated emission depletion microscopy [2]. Also nonclassical features such as entanglement [3], quantum interferometry [4], or multiphoton processes [5] can be used to enhance resolution. Somewhat complementary to this, a particularly promising development is lensless near-field optics, which can achieve nanometer spatial resolution [6].

On the other hand, the resonance fluorescence emitted collectively by many interacting two-level atoms in an external driving laser field has been studied extensively for different parameter ranges [7–14]. Following the idea of reaching subwavelength resolution for nonidentical, individually addressable objects [15], a relation between collective fluorescent light and the geometry of the setup was also shown experimentally [16].

In our previous work [17], motivated by the localization of an atom inside an optical field [18], we showed that distance and position information can be obtained by measuring the fluorescence spectrum of a two-atom system inside a standing-wave field, relying entirely on far-field measurement techniques. Typically, this scheme will be limited by the difficulties in fixing the positions of the two atoms rather than by constraints of the measurement scheme itself, which in principle allows one to achieve resolution far below the classical Rayleigh limit of optical microscopy technology.

In addition to the fluorescence spectrum, also the intensity-intensity correlation function of the light emitted by

a collection of two- and three-level atom systems subject to driving fields has been investigated [12,13,19–21]. Most of these works, however, focused on nonclassical properties of the emitted field. Thus the question arises: Does the intensity-intensity correlation function also reveal information about the spatial properties of a given system? In [12], the effect of the interatomic distance on the intensity-intensity correlation function of the resonance fluorescence of two atoms is mentioned. However, that analysis of the intensity-intensity correlation function focuses on the case when the collective damping rate is exactly equal to the Einstein  $A$  coefficient of a single atom. Here, we consider a more realistic situation without any significant restrictions on the damping rate.

We present a detailed analysis of the application of the intensity-intensity correlation functions to the potential microscopy and atom imaging. We include in our analysis the dipole-dipole interaction between atoms. In particular, we demonstrate how the distance information can be obtained by measuring the intensity-intensity correlation function of the emitted fluorescence field. It turns out that the power spectrum of the intensity-intensity correlation function is well suited to gaining distance information over a wide range of parameters with high accuracy. Our results can be applied to physical systems which may be approximated as two-level systems, where the two energy states are connected by an electric-dipole-allowed transition. Possible examples include atoms, molecules, and artificial quantum systems such as quantum dots.

This paper is organized as follows. First, we give a brief description of the system and derive expressions for the intensity-intensity correlation function. Next, we discuss the dependence of the correlation function on the interatomic distance based on the numerical results. Finally, based on these results, we propose a measurement scheme that allows us to obtain distance information from the correlation function and its power spectrum.

**II. INTENSITY-INTENSITY CORRELATION FUNCTION**

Our model system consists of two identical two-level atoms, with transition frequencies  $\omega_0$ , dipole transition mo-

\*Electronic address: [zubairy@physics.tamu.edu](mailto:zubairy@physics.tamu.edu)

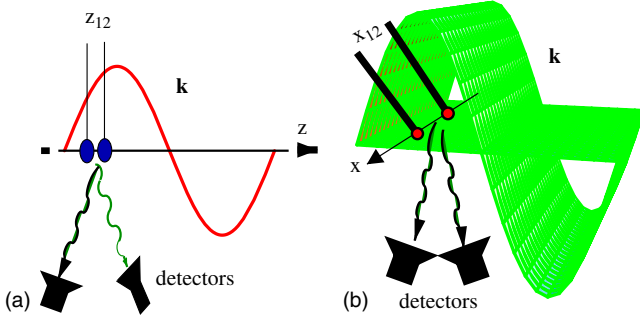


FIG. 1. (Color online) Two atoms in a standing-wave field with a distance  $r_{ij}$  smaller than half the wavelength  $\lambda/2$  of the driving field. Two geometries are considered in this paper: The driving field propagation direction is either (a) parallel or (b) perpendicular to the interatomic distance vector  $\mathbf{r}_{12}$ .

ment  $\mu$ , and decay rate  $\gamma$ . The atoms are assumed to be located at position  $\mathbf{r}_i = (x_i, y_i, z_i)^T$  in a linearly polarized near-resonant standing-wave laser field [see Fig. 1(a)]. The distance between them is  $r_{12} = |\mathbf{r}_{12}|$  with  $\mathbf{r}_{ij} = \mathbf{r}_i - \mathbf{r}_j$ . Further, they are coupled to all the other modes of the electromagnetic field, which are assumed to be in their vacuum state initially.

In the laboratory frame and under the rotating-wave approximation, the system evolution is described by the reduced atomic density operator  $\rho$ , which obeys the following master equation [22–25]:

$$\frac{\partial \rho}{\partial t} = \frac{1}{i\hbar} [H, \rho] - \sum_{i,j=1}^2 \gamma_{ij} ([S_i^+, S_j^- \rho] - [S_j^-, \rho S_i^+]). \quad (1)$$

Here  $S_i^+$  and  $S_i^-$  are the atomic raising and lowering operators that raise and lower the state of atom  $i$  ( $i \in \{1, 2\}$ ). These operators satisfy the following relations ( $i \neq j$ ):

$$(S_i^\pm)^2 = 0, \quad S_i^\pm S_j^\pm = S_j^\pm S_i^\pm, \quad S_i^\pm S_j^\mp = S_j^\mp S_i^\pm. \quad (2)$$

The system Hamiltonian is given by  $H = H_0 + H_{dd} + H_L$ , where

$$H_0 = \frac{\hbar}{2} \omega_0 \sum_{i=1}^2 (S_i^+ S_i^- - S_i^- S_i^+), \quad (3)$$

$$H_{dd} = \hbar \Omega_{12} (S_1^+ S_2^- + S_2^+ S_1^-), \quad (4)$$

$$H_L = \frac{\hbar}{2} \sum_{i=1}^2 (\Omega_i S_i^+ e^{-i\omega_L t} + \text{H.c.}) \quad (5)$$

are the free energy, the dipole-dipole interaction, and the interaction with the driving laser field, respectively. In the above equations,  $\omega_L$  is the frequency of the driving field and  $\mathbf{k} = k\hat{\mathbf{k}}$  is its wave vector, which is along the  $z$  axis of our coordinate frame.  $\Omega_i$  is the driving-field Rabi frequency of atom  $i$  ( $i \in \{1, 2\}$ ). The parameter  $\gamma_{ij}$  is given by

$$\gamma_{ij} = \frac{3}{2} \gamma \left( \frac{\sin(kr_{ij})}{(kr_{ij})} + \frac{\cos(kr_{ij})}{(kr_{ij})^2} - \frac{\sin(kr_{ij})}{(kr_{ij})^3} \right), \quad (6)$$

and contains both the usual spontaneous emission rates  $\gamma$  of the two individual atoms ( $i=j$ ) and collective cross-damping

terms ( $i \neq j$ ). The dipole-dipole interaction potential  $\Omega_{12}$  is given by

$$\Omega_{12} = \frac{3}{2} \gamma \left( -\frac{\cos(kr_{12})}{(kr_{12})} + \frac{\sin(kr_{12})}{(kr_{12})^2} + \frac{\cos(kr_{12})}{(kr_{12})^3} \right). \quad (7)$$

Both the terms proportional to  $\Omega_{12}$  and  $\gamma_{12}$  in the master equation (1) arise from the interaction of the atoms via the empty modes of the quantized radiation field [9]. From Eqs. (6) and (7), we can see that these two dipole-dipole interaction terms can crucially influence the system dynamics if the two atoms are very close to each other. For small interatomic distances ( $kr_{12} \ll 1$ ), Eqs. (6) and (7) may be simplified to

$$\Omega_{12} \approx \frac{3\gamma}{2(kr_{12})^3}, \quad \gamma_{ij} \approx \gamma. \quad (8)$$

For large distances ( $kr_{12} \gg 1$ ),  $\Omega_{12} \approx 0$  and  $\gamma_{ij} \approx \gamma \delta_{ij}$ , where  $\delta_{ij}$  is the Kronecker delta symbol.

Supposing that the laser propagation direction is along the interatomic distance vector, and that the position of the first atom relative to a standing-wave field node is  $z_1$ , then the two Rabi frequencies are given by

$$\Omega_1 = \Omega \sin(kz_1), \quad \Omega_2 = \Omega \sin(kz_{12} + kz_1), \quad (9)$$

where  $z_{12} = r_{12}$  in our geometry. Further, we suppose that the transition dipole moments of the two atoms are parallel to each other and are aligned perpendicular to the distance vector of the two atoms  $\mathbf{r}_{12}$ , e.g., by means of a weak external field. Note that in other geometries, further contributions to the master equation may arise [26]. The geometry of the system is illustrated in Fig. 1(a).

The two-time intensity-intensity correlation function of the light field detected at point  $\mathbf{R}_1$  at time  $t_1$  and at a point  $\mathbf{R}_2$  at time  $t_2$  is defined as [27]

$$G^{(2)}(\mathbf{R}_1, t_1; \mathbf{R}_2, t_2) = \langle E^{(-)}(\mathbf{R}_1, t_1) E^{(-)}(\mathbf{R}_2, t_2) E^{(+)}(\mathbf{R}_2, t_2) \times E^{(+)}(\mathbf{R}_1, t_1) \rangle. \quad (10)$$

Here,  $E^{(\pm)}$  are the negative- and positive-frequency parts of the electric field operator. The normalized intensity-intensity correlation function is defined as

$$g^{(2)}(\mathbf{R}_1, t_1; \mathbf{R}_2, t_2) = \frac{G^{(2)}(\mathbf{R}_1, t_1; \mathbf{R}_2, t_2)}{G^{(1)}(\mathbf{R}_1, t_1) G^{(1)}(\mathbf{R}_2, t_2)}, \quad (11)$$

where

$$G^{(1)}(\mathbf{R}_i, t_i) = \langle E^{(-)}(\mathbf{R}_i, t_i) E^{(+)}(\mathbf{R}_i, t_i) \rangle \quad (12)$$

is the first-order correlation function of the field detected at a point  $\mathbf{R}_i$  at time  $t_i$  ( $i \in \{1, 2\}$ ), i.e., the field intensity. The correlation function  $G^{(2)}(\mathbf{R}_1, t_1; \mathbf{R}_2, t_2)$  is proportional to the joint probability of finding one photon at  $\mathbf{R}_1$  at time  $t_1$  and another photon at  $\mathbf{R}_2$  at time  $t_2$ , and yields information about the photon statistics of the emitted light.

Following the approach in [27], these two kinds of correlation functions can be written in terms of the expectation values of the atomic transition operators as follows:

$$G^{(1)}(\mathbf{R}, t) = U(\mathbf{R}) \sum_{i,j=1}^2 \langle S_i^+(t') S_j^-(t') \rangle \exp(ik\hat{\mathbf{R}} \cdot \mathbf{r}_{ij}), \quad (13)$$

$$G^{(2)}(\mathbf{R}_1, t_1; \mathbf{R}_2, t_2) = U(\mathbf{R}_1)U(\mathbf{R}_2) \times \sum_{i,j,k,l=1}^2 \langle S_i^+(t_1^{(i)})S_j^+(t_2^{(j)})S_k^-(t_2^{(k)})S_l^-(t_1^{(l)}) \rangle \times \exp[ik(\hat{\mathbf{R}}_1 \cdot \mathbf{r}_{il} + \hat{\mathbf{R}}_2 \cdot \mathbf{r}_{jk})], \quad (14)$$

where  $t' = t - R/c$ ,  $t_i^{(\alpha)} = t_i - R_\alpha/c$ , and  $U(\mathbf{R}_i) = \omega_0^4 \mu^2 \sin^2 \theta / (2\mathbf{R}_i^2 \pi \epsilon_0)$  ( $i, \alpha \in \{1, 2\}$ ). Here,  $\theta$  is the angle between the observation direction and the atomic dipole moment  $\mu$ . Note that we do not include retardation effects, since it has been shown that retardation effects play a significant role in the resonant interaction of two identical atoms only if the interatomic distance is larger than the resonant wavelength [28].

Thus, the normalized intensity-intensity correlation function of the steady state can be written as

$$g^{(2)}(\mathbf{R}_1, \mathbf{R}_2; \tau) = \lim_{t_1 \rightarrow \infty} g^{(2)}(\mathbf{R}_1, t_1; \mathbf{R}_2; t_1 + \tau) = \lim_{t_1 \rightarrow \infty} \frac{G^{(2)}(\mathbf{R}_1, t_1; \mathbf{R}_2, t_1 + \tau)}{G^{(1)}(\mathbf{R}_1, t_1) \cdot G^{(1)}(\mathbf{R}_2, t_1 + \tau)}. \quad (15)$$

In our geometry, under the far-field approximation, we have

$$R_1 = R_2, \quad (16)$$

$$t_1^{(1)} = t_1^{(2)} = t_1', \quad (17)$$

$$t_2^{(1)} = t_2^{(2)} = t_2'. \quad (18)$$

Therefore the intensity-intensity correlation function can be simplified to give

$$g^{(2)}(\mathbf{R}_1, \mathbf{R}_2; \tau) = \lim_{t_1' \rightarrow \infty} \sum_{i,j,k,l=1}^2 e^{ik(\hat{\mathbf{R}}_1 \cdot \mathbf{r}_{il} + \hat{\mathbf{R}}_2 \cdot \mathbf{r}_{jk})} \times \frac{\langle S_i^+(t_1')S_j^+(t_1' + \tau)S_k^-(t_1' + \tau)S_l^-(t_1') \rangle}{\left( \sum_{m,n=1}^2 \langle S_m^+(t_1')S_n^-(t_1') \rangle \exp(ik\hat{\mathbf{R}} \cdot \mathbf{r}_{mn}) \right)^2}. \quad (19)$$

Thus, we have expressed the correlation function of the electromagnetic field in terms of the correlation function of atomic operators. It is well known that the expectation value of an atomic operator  $Q$  can be written as

$$\langle Q \rangle = \text{Tr}_s(\rho Q), \quad (20)$$

where the trace involves only atomic and laser field degrees of freedom. Substituting  $S_i^\pm (i \in \{1, 2\})$  into Eq. (20) and using the master equation (1), we can get a closed set of 15 first-order differential equations describing the evolution of the atomic variables. In a matrix notation, this set of equations can be rewritten as an inhomogeneous equation:

$$\dot{\mathbf{X}}(t) = \mathbf{M}\mathbf{X}(t) + \mathbf{I}, \quad (21)$$

where the overdot indicates differentiation with respect to  $\gamma t$ .  $\mathbf{X}(t)$  is the column vector with elements

$$X_1 = \langle \tilde{S}_1^+ \rangle, \quad X_2 = \langle \tilde{S}_1^- \rangle, \quad (22a)$$

$$X_3 = \langle \tilde{S}_2^+ \rangle, \quad X_4 = \langle \tilde{S}_2^- \rangle, \quad (22b)$$

$$X_5 = \langle \tilde{S}_1^+ \tilde{S}_1^- \rangle, \quad X_6 = \langle \tilde{S}_2^+ \tilde{S}_2^- \rangle, \quad (22c)$$

$$X_7 = \langle \tilde{S}_1^+ \tilde{S}_2^- \rangle, \quad X_8 = \langle \tilde{S}_2^+ \tilde{S}_1^- \rangle, \quad (22d)$$

$$X_9 = \langle \tilde{S}_1^+(t) \tilde{S}_2^+ \rangle, \quad X_{10} = \langle \tilde{S}_1^- \tilde{S}_2^- \rangle, \quad (22e)$$

$$X_{11} = \langle \tilde{S}_1^+ \tilde{S}_1^- \tilde{S}_2^- \rangle, \quad X_{12} = \langle \tilde{S}_1^+ \tilde{S}_2^+ \tilde{S}_1^- \rangle, \quad (22f)$$

$$X_{13} = \langle \tilde{S}_2^+ \tilde{S}_1^- \tilde{S}_2^- \rangle, \quad X_{14} = \langle \tilde{S}_1^+ \tilde{S}_2^+ \tilde{S}_2^- \rangle, \quad (22g)$$

$$X_{15} = \langle \tilde{S}_1^+ \tilde{S}_2^+ \tilde{S}_1^- \tilde{S}_2^- \rangle. \quad (22h)$$

The operators in Eq. (22) are defined as

$$\tilde{S}_i^\pm(t) = S_i^\pm \exp(\mp i\omega_L t). \quad (23)$$

$\mathbf{M}$  is a  $15 \times 15$  matrix containing the coefficients of the differential equations, and  $\mathbf{I}$  is a constant column vector. The nonvanishing elements of matrix  $\mathbf{M}$  and vector  $\mathbf{I}$  are given in the Appendix. The dimensionless parameters are defined as

$$\beta_1 = \frac{\Omega_1}{\gamma}, \quad \beta_2 = \frac{\Omega_2}{\gamma}, \quad a = \frac{\gamma_{12}}{\gamma}, \quad (24a)$$

$$b = \frac{\Omega_{12}}{\gamma}, \quad \Delta = \frac{(\omega_L - \omega_0)}{\gamma}. \quad (24b)$$

For nonzero determinant of the matrix  $\mathbf{M}$ , the steady-state solution of Eq. (21) is given by

$$\mathbf{X}(\infty) = -\mathbf{M}^{-1}\mathbf{I}. \quad (25)$$

Then the matrix  $\mathbf{M}$  can be diagonalized by a complex invertible matrix  $\mathbf{T}$ . Let  $\mathbf{q} = \mathbf{T}^{-1}\mathbf{M}\mathbf{T}$ ,  $\mathbf{Y} = \mathbf{T}^{-1}\mathbf{X}$ , and  $\mathbf{W} = \mathbf{T}^{-1}\mathbf{I}$ , then the solution of Eq. (21) can be rewritten as

$$Y_i(\tau) = \lim_{t \rightarrow \infty} [Y_i(t)] \exp(\mathbf{q}_{ii}\tau) - (\mathbf{q}^{-1})_{ii} [1 - \exp(\mathbf{q}_{ii}\tau)] W_i. \quad (26)$$

In order to calculate the two-time correlation function, we also need to make use of the quantum regression theorem [24]. It states that for some operator  $\hat{O}$ , if the time evolution of one-time expectation values can be written as

$$\langle \hat{O}(t + \tau) \rangle = \sum_j a_j(\tau) \langle \hat{O}_j(t) \rangle, \quad (27)$$

then two-time expectation values can be expressed as

$$\langle \hat{O}_i(t) \hat{O}(t + \tau) \hat{O}_k(t) \rangle = \sum_j a_j(\tau) \langle \hat{O}_i(t) \hat{O}_j(t) \hat{O}_k(t) \rangle. \quad (28)$$

With this preparatory knowledge, we can express the steady state of the first- and second-order correlation functions of the radiation field as follows:

$$G^{(1)}(\mathbf{R}, t)^{SS} = X_\alpha + X_\beta \cos(k\hat{\mathbf{R}} \cdot \mathbf{r}_{12}) + iX_\gamma \sin(k\hat{\mathbf{R}} \cdot \mathbf{r}_{12}), \quad (29)$$

and

$$\begin{aligned} G^{(2)}(\mathbf{R}_1, \mathbf{R}_2, \tau)^{SS} = & [X_\alpha + X_\beta \cos(k\hat{\mathbf{R}}_1 \cdot \mathbf{r}_{12}) \\ & + iX_\gamma \sin(k\hat{\mathbf{R}}_1 \cdot \mathbf{r}_{12})][X_\alpha \\ & + X_\beta \cos(k\hat{\mathbf{R}}_2 \cdot \mathbf{r}_{12}) \\ & + iX_\gamma \sin(k\hat{\mathbf{R}}_2 \cdot \mathbf{r}_{12})] \\ & + \sum_{j=1}^{15} P_j e^{q_{jj}\tau}. \end{aligned} \quad (30)$$

Here,  $X_\alpha = X_5(\infty) + X_6(\infty)$ ,  $X_\beta = X_7(\infty) + X_8(\infty)$ , and  $X_\gamma = X_7(\infty) - X_8(\infty)$ ; superscript *SS* indicates steady-state results. Further

$$\begin{aligned} P_j = & [A_j + B_j + (C_j + D_j)\cos(k\hat{\mathbf{R}}_1 \cdot \mathbf{r}_{12}) + i(C_j - D_j) \\ & \times \sin(k\hat{\mathbf{R}}_1 \cdot \mathbf{r}_{12})][(T_{5j} + T_{6j}) + (T_{7j} + T_{8j}) \\ & \times \cos(k\hat{\mathbf{R}}_1 \cdot \mathbf{r}_{12}) + i(T_{7j} - T_{8j})\sin(k\hat{\mathbf{R}}_1 \cdot \mathbf{r}_{12})], \end{aligned} \quad (31)$$

where

$$\begin{aligned} A_j = & (T^{-1})_{j3}X_{12}(\infty) + (T^{-1})_{j4}X_{11}(\infty) + (T^{-1})_{j6}X_{15}(\infty) \\ & + (\mathbf{q}^{-1})_{jj}W_jX_5(\infty), \end{aligned} \quad (32a)$$

$$\begin{aligned} B_j = & (T^{-1})_{j1}X_{12}(\infty) + (T^{-1})_{j2}X_{13}(\infty) + (T^{-1})_{j5}X_{15}(\infty) \\ & + (\mathbf{q}^{-1})_{jj}W_jX_6(\infty), \end{aligned} \quad (32b)$$

$$\begin{aligned} C_j = & (T^{-1})_{j2}X_{11}(\infty) + (T^{-1})_{j3}X_{14}(\infty) + (T^{-1})_{j8}X_{15}(\infty) \\ & + (\mathbf{q}^{-1})_{jj}W_jX_7(\infty), \end{aligned} \quad (32c)$$

$$\begin{aligned} D_j = & (T^{-1})_{j1}X_{12}(\infty) + (T^{-1})_{j4}X_{13}(\infty) + (T^{-1})_{j7}X_{15}(\infty) \\ & + (\mathbf{q}^{-1})_{jj}W_jX_8(\infty). \end{aligned} \quad (32d)$$

### III. NUMERICAL RESULT AND DISTANCE MEASUREMENT

Using Eq. (30), we can numerically calculate the normalized intensity-intensity correlation function  $g^{(2)}(\tau)$ . The results show very distinct behavior for different interatomic distance ranges. Figure 2 shows several examples of the correlation function  $g^{(2)}(\tau)$  for different interatomic distances, with the parameters indicated there.

It turns out that the intensity-intensity correlation function itself cannot easily be interpreted in terms of the actual interatomic distance. Instead, it is more convenient to analyze the power spectrum of the intensity-intensity correlation functions. For simplicity, the power spectrum of  $g^{(2)}(\tau) - 1$  is studied here. As  $\lim_{\tau \rightarrow \infty} g^{(2)}(\tau) = 1$ , the constant only gives rise to a  $\delta$  peak contribution at a frequency of zero in the power spectrum of  $g^{(2)}(\tau)$ . From Eq. (30), it is easy to evaluate the Fourier transform of  $g^{(2)}(\tau) - 1$  as

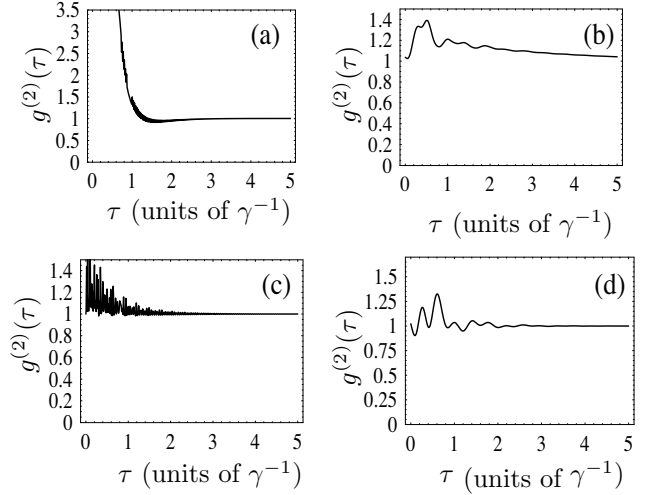


FIG. 2. Samples of  $g^{(2)}(\tau)$  for  $\Delta=0$ ,  $\hat{\mathbf{R}}_1 \cdot \mathbf{r}_{12} = \hat{\mathbf{R}}_2 \cdot \mathbf{r}_{12} = 0$ ,  $kz_1 = 0.1\pi$ . (a) Small-distance case:  $z_{12} = 0.03\lambda$ ,  $\Omega = 20\gamma$ . (b) Intermediate distance, weak driving field:  $z_{12} = 0.08\lambda$ ,  $\Omega = 20\gamma$ . (c) Intermediate distance, strong driving field:  $z_{12} = 0.08\lambda$ ,  $\Omega = 300\gamma$ . (d) Large-distance case:  $z_{12} = 0.6\lambda$ ,  $\Omega = 20\gamma$ .

$$\begin{aligned} S(\nu) = & \frac{1}{\mathcal{N}} \sum_{j=1}^{15} \left( \frac{iP_j}{\nu + \text{Im}(q_{jj}) - i \text{Re}(q_{jj})} \right. \\ & \left. + \frac{iP_j^*}{\nu - \text{Im}(q_{jj}) - i \text{Re}(q_{jj})} \right). \end{aligned} \quad (33)$$

Here,  $\mathcal{N} = 2\sqrt{2\pi} [G^{(1)}(\mathbf{R}, \infty)]^2$  is a normalization constant, and  $\text{Im}(x)$  and  $\text{Re}(x)$  denote the imaginary and the real part of  $x$ , respectively. The power spectrum  $|S(\nu)|$  is shown in Figs. 3–6, with same parameters as in Fig. 2. With the help of Figs. 3–6, it is clear that the different behaviors of the intensity-intensity correlation functions are due to different frequency components dominating the system. These frequency components are related to the position and distance information of the two atoms. With the help of Eq. (33), we can use the two atomic position parameters  $z_1$  and  $z_{12}$  to fit the measured correlation function and spectrum using well-developed experimental data analysis techniques. This process provides the position and distance information between the two atoms.

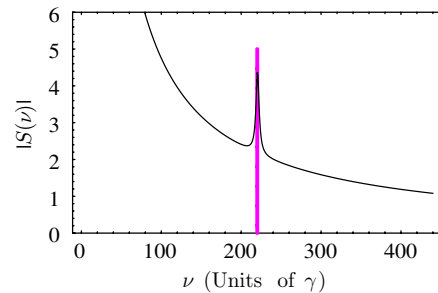


FIG. 3. (Color online) Power spectrum of the  $g^{(2)}(\tau)$  sample shown in Fig. 2(a), the small-distance case:  $z_{12} = 0.03\lambda$ ,  $\Omega = 20\gamma$ . The solid line indicates the position of  $\Omega_{12}$ .

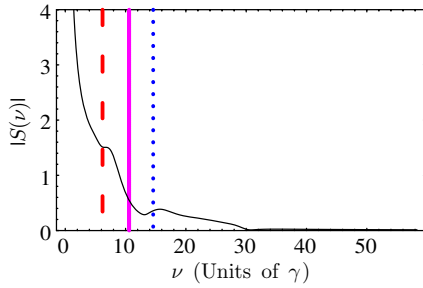


FIG. 4. (Color online) Power spectrum of the  $g^{(2)}(\tau)$  sample shown in Fig. 2(b), for the case of intermediate distance and weak driving field:  $z_{12}=0.08\lambda$ ,  $\Omega=20\gamma$ . The solid line indicates the position of  $\Omega_{12}$ , the dashed line indicates the position of  $\Omega_1$ , and the dotted line indicates the position of  $\Omega_2$ .

Thus the basic strategy is to measure the intensity-intensity correlation function of the resonance fluorescence light field, to evaluate the power spectrum from it, and then to extract spatial information from it by fitting it numerically. However, our investigation of the properties of  $g^{(2)}(\tau)$  and  $|S(\nu)|$  shows that in certain limiting cases, it is possible to obtain the distance and position information directly from the power spectrum with satisfactory precision, i.e., without the fitting of the full spectrum. This will be discussed together with the measurement procedure in the following.

The first step is to apply a standing-wave laser field to the two-atom system, which corresponds to a maximum Rabi frequency  $\Omega$  of about  $20\gamma$  for an atom positioned at an antinode of the standing wave. The laser propagation direction is along the connection vector  $\mathbf{r}_{12}$  of the two atoms. Since we are measuring in the far-field region such that the interatomic distance is much smaller than the distance from the atoms to the detectors, we can always arrange the two photon detectors at positions  $\mathbf{R}_1$  and  $\mathbf{R}_2$  with  $R_1=R_2$  and directions perpendicular to the interatomic distance vector ( $\mathbf{R}_1 \perp \mathbf{r}_{12}$ ,  $\mathbf{R}_2 \perp \mathbf{r}_{12}$ ). Using coincidence measurement techniques, the intensity-intensity correlation function of the emitted light field can be measured. Based on the results of the  $g^{(2)}(\tau)$  measurement, three different parameter ranges can be distinguished.

(a) If  $g^{(2)}(\tau)$  and its power spectrum are similar to those in Figs. 2(a) and 3, then the interatomic distance is small ( $z_{12}$

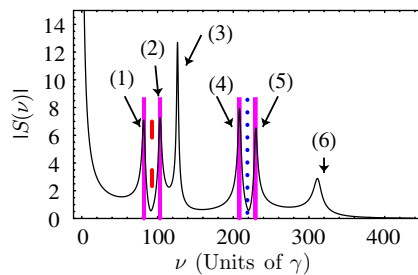


FIG. 5. (Color online) Power spectrum of the  $g^{(2)}(\tau)$  sample shown in Fig. 2(c), for the case of intermediate distance and strong driving field:  $z_{12}=0.08\lambda$ ,  $\Omega=300\gamma$ . The solid lines indicate the positions of  $\Omega_1 \pm \Omega_{12}$  and  $\Omega_2 \pm \Omega_{12}$ , the dashed line indicates the position of  $\Omega_1$ , and the dotted line indicates the position of  $\Omega_2$ . In the spectrum, the peaks 1, 2, 3, 4, 5, and 6 correspond to frequencies  $\Omega_1 - \Omega_{12}$ ,  $\Omega_1 + \Omega_{12}$ ,  $\Omega_2 - \Omega_{12}$ ,  $\Omega_2 + \Omega_{12}$ ,  $\Omega_1 + \Omega_{12}$ , and  $\Omega_1 + \Omega_{12}$ .

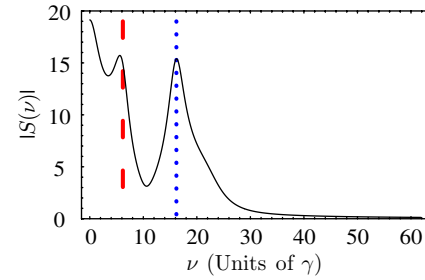


FIG. 6. (Color online) Power spectrum of the  $g^{(2)}(\tau)$  sample shown in Fig. 2(d), the large-distance case:  $z_{12}=0.6\lambda$ ,  $\Omega=20\gamma$ . The dashed line indicates the position of  $\Omega_1$ , and the dotted line indicates the position of  $\Omega_2$ .

$\leq \lambda/30$ ). In Figs. 2(a) and 3, the actual interatomic distance is  $z_{12}=0.03\lambda$ , which corresponds to an interaction energy of  $\Omega_{12}=220.096\gamma$ . The system evolution is dominated by the dipole-dipole interaction energy  $\Omega_{12}$ , which gives rise to a single-peak structure in the  $g^{(2)}$  spectrum. As shown in Fig. 3, the peak center  $\nu_p$  is coincident with the dipole-dipole interaction coefficient  $\Omega_{12}$  indicated by a solid line. Thus, a measurement of the peak position  $\nu_p$  allows us to gain an estimate of  $\Omega_{12}$  and thus of the interatomic distance via Eq. (7).

In a measurement, two error sources have to be distinguished. The first error source is related to experimental imperfections, and corresponds to uncertainties in the measurement of the spectra shown in Figs. 3–6. In the following, for simplicity, we will cover such uncertainties by an overall relative experimental uncertainty  $U^{expt}$ . The position of the peak in the spectrum Fig. 3 is  $\nu_p=220.49\gamma$ . Assuming an experimental uncertainty of  $U^{expt}=10\%$ , the experimentally accessible value for  $\Omega_{12}$  thus is  $\Omega_{12}^{expt}=(220.49 \pm 22.05)\gamma$ . From Eq. (7),  $\Omega_{12}^{expt}$  yields a measured distance of  $z_{12}^{expt}=(0.030 \pm 0.001)\lambda$ , which is in very good agreement with the actual value  $z_{12}=0.03\lambda$ . Note that due to the structure of Eq. (7), for small distances, the experimental uncertainty of  $z_{12}^{expt}$  is only about  $U^{expt}/3$  [17]. In this example, the absolute measurement uncertainty for the distance is less than 0.4% of the wavelength  $\lambda$ .

The second source is a systematic error, and is due to the fact that the peak position  $\nu_p$  accessible in experiments does not exactly coincide with the theoretical interaction energy  $\Omega_{12}$ . This deviation is generally negligible for small interatomic distances, but will be discussed below in this section.

If we look more closely at the details of the peak in Fig. 3, it reveals a more complicated structure. In Fig. 7, it can be seen that the dominating peak is overlaid by a Fano-like “spike” structure. One way of avoiding such complications is to adjust the geometry of the system to the setup in Fig. 1(b), where the driving field propagates perpendicular to the interatomic distance vector of the two atoms. In this configuration, the two atoms experience the same driving field ( $\Omega_1=\Omega_2$ ). This symmetry simplifies the power spectrum of  $g^{(2)}$ , as shown in Fig. 8. On the other hand, resolving this structure in an experiment may provide a more accurate measurement of the interatomic distance, as discussed in the next paragraph.

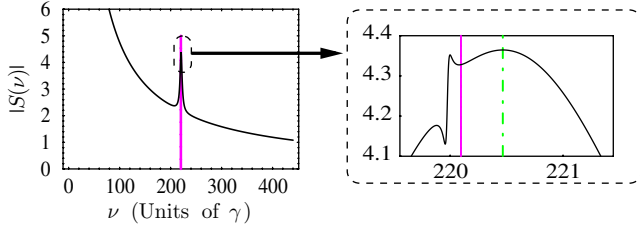


FIG. 7. (Color online) Detailed spectrum for small interatomic distances under different alignments (cf. Fig. 8). The two atoms are aligned along the propagation direction of the driving field, as shown in Fig. 1(a). In the enlargements, solid vertical line indicates the actual value of  $\Omega_{12}$ , whereas the dashed line indicates the peak center of the plotted spectrum.

We now turn to a more thorough study of the deviation of the experimentally accessible peak position  $\nu_p$  from the theoretical value of  $\Omega_{12}$  in the geometry described in Fig. 1(a). Figure 9 shows this relative deviation  $U_d = (\nu_p - \Omega_{12})/\Omega_{12}$  versus the atomic separation  $z_{12}$  for different Rabi frequencies  $\Omega$  of the driving field. Figure 10 shows the deviation  $U_d$  versus the Rabi frequency for different positions of the first atom. It is apparent that as long as  $\Omega, \gamma \ll \Omega_{12}$  is satisfied, the peak position  $\nu_p$  can directly be identified with  $\Omega_{12}$ ; the deviation  $U_d$  is much smaller than 1%. If for a specific setup the experimental uncertainties  $U^{expt}$  are smaller than  $U_d$ , then the accuracy of the distance measurement can be maximized by fitting the whole  $g^{(2)}$  spectrum numerically, taking the approximate results of the above scheme as a starting point. In Figs. 9 and 10, we also find branching points similar to those found in our previous work [17]. However, it is very difficult to get accurate analytic relations between the positions of the branching points and the system parameters of interest without a numerical fit. Therefore, here we only focus on the distance information. One can, however, also take advantage of the “spike” as shown in Fig. 7 instead of avoiding it by switching to a new alignment. A numerical investigation shows that the position  $\nu_d$  of the dip behind this spike is much closer to  $\Omega_{12}$  than the peak position  $\nu_p$  found in the previous part. For example, in Fig. 7, one finds  $\nu_d = 220.079\gamma$ , such that the deviation from  $\Omega_{12}$  is only 0.008%. This is significantly less than the deviation between  $\nu_p$  and  $\Omega_{12}$ , which is approximately 0.17%. Thus the systematic error  $U_d$  of this method is very small, and the error of the

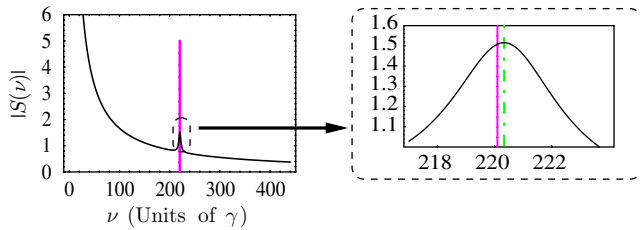


FIG. 8. (Color online) Detailed spectrum for small interatomic distances under different alignments (cf. Fig. 7). The interatomic distance vector is perpendicular to the laser propagation direction, as shown in Fig. 1(b). In the enlargements, solid vertical line indicates the actual value of  $\Omega_{12}$ , whereas the dashed line indicates the peak center of the plotted spectrum.

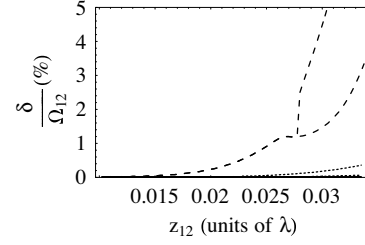


FIG. 9. Deviation  $\delta/\Omega_{12} = (\nu_p - \Omega_{12})/\Omega_{12}$  of the peak position  $\nu_p$  from  $\Omega_{12}$  for closely spaced atoms in the geometry shown in Fig. 1(a) ( $\Delta = 0, \hat{\mathbf{R}}_1 \cdot \mathbf{r}_{12} = \hat{\mathbf{R}}_2 \cdot \mathbf{r}_{12} = 0$ ), and plotted against the interatomic separation.  $kz_1 = 0.1\pi$ ,  $\Omega = 3\gamma$  (solid),  $20\gamma$  (dotted),  $80\gamma$  (dashed). Branches correspond to splittings into two peaks.

final result will be dominated by the other error sources summarized in  $U^{expt}$ .

(b) If the measured  $g^{(2)}(\tau)$  and its power spectrum are similar to those in Figs. 2(b) and 4, then the interatomic distance is in the range  $\lambda/30 - \lambda/10$ , which we call the “intermediate-distance case.” In this regime, the effects of the driving field and the dipole-dipole interaction between the two atoms are comparable to each other. As a result, the correlation function and its power spectrum are rather complicated. All frequency components related to these two interactions and their combinations show up in the power spectrum. One way of avoiding this complication is to increase the intensity of the driving field, typically such that the maximum Rabi frequency reaches about  $200\gamma$ . While the driving-field intensity is increased, one continuously measures the intensity-intensity correlation function and its power spectrum. Eventually, the spectrum looks like Fig. 5, where all the frequency peaks are well separated, and there are two doublets which maintain the same doublet splitting  $\sigma_s$  during the increase of the field intensity. These doublets can be identified with the frequencies  $\Omega_1 \pm \Omega_{12}$  and  $\Omega_2 \pm \Omega_{12}$ . For example, in Fig. 5, the theoretical value for  $2\Omega_{12}$  is  $21.189\gamma$ , corresponding to an actual value of  $z_{12} = 0.08\lambda$ . On the other hand, the experimentally accessible splitting of the doublet around  $\Omega_1$  is  $\sigma_s = 21.63\gamma$ . Allowing for an experimental uncertainty  $U^{expt} = 5\%$ , the measured splitting thus is  $2\Omega_{12}^{expt} = (21.63 \pm 1.1)\gamma$ . Using Eq. (7), the measured interatomic distance evaluates to  $z_{12}^{expt} = (0.079 \pm 0.0014)\lambda$ , which again is in good agreement with the actual value.

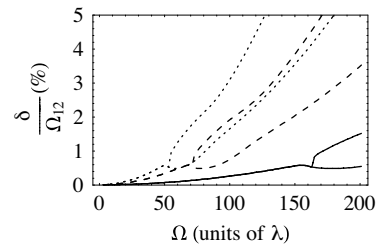


FIG. 10. Deviation  $\delta/\Omega_{12} = (\nu_p - \Omega_{12})/\Omega_{12}$  of the peak position  $\nu_p$  from  $\Omega_{12}$  for closely spaced atoms in the geometry shown in Fig. 1(a) ( $\Delta = 0, \hat{\mathbf{R}}_1 \cdot \mathbf{r}_{12} = \hat{\mathbf{R}}_2 \cdot \mathbf{r}_{12} = 0$ ), and plotted against the driving field Rabi frequency.  $z_{12} = 0.02\lambda$ ,  $kz_1 = 0.1\pi$  (dotted),  $0.25\pi$  (solid),  $0.4\pi$  (dashed). Branches correspond to splittings into two peaks.

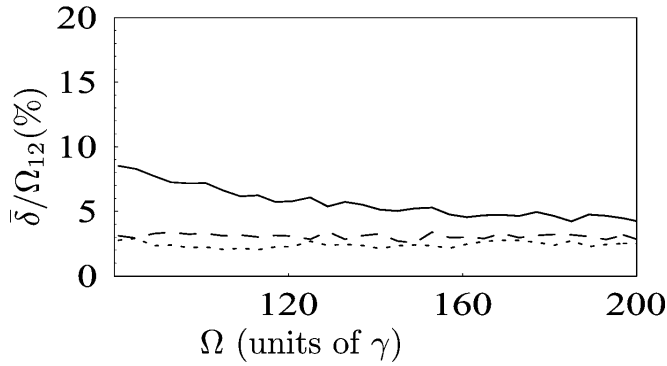


FIG. 11. Deviation  $\bar{\delta} = \sigma_p - 2\Omega_{12}$  of the doublet splitting  $\sigma_p$  from  $2\Omega_{12}$  for the strong-field, intermediate-distance case.  $r_{12} = 0.08\lambda$ ,  $\theta = \pi/2$ , and  $\Delta = 0$ . The positions of the atoms are  $kz_1 = 0.1\pi$  (solid),  $0.2\pi$  (dashed), and  $0.3\pi$  (dotted).

We now turn to the discussion of the systematic error sources in this case. Figure 11 shows the relative deviation  $U_d = (\nu_p - \Omega_{12})/\Omega_{12}$  of the experimentally accessible doublet splitting  $\sigma_s$  from the desired value  $2\Omega_{12}$  versus the driving field Rabi frequency for different position of the first atom. It can be seen that this deviation can be kept less than 5%, if the driving field is strong enough ( $\Omega \gg \Omega_{12}$ ). Apart from increasing the intensity of the driving field, the field phase can also be adjusted such that the atoms come close to a node. Then, the effective Rabi frequencies  $\Omega_1$  and  $\Omega_2$  increase. Again, more accurate information can be obtained by a numerical fit of the measured spectrum, starting from the approximate values obtained via the above scheme.

(c) Finally, if  $g^{(2)}(\tau)$  and its power spectrum are similar to those in Figs. 2(d) and 6, it means that the interatomic distance is much larger than in the previous two cases. Here we suppose that the two atoms are confined to within one quarter of a wavelength, as larger distances are accessible by classical measurement schemes, or by the scheme considered in our previous work [17]. For larger distances, the dipole-dipole interaction is very small. The system is dominated by the interaction between the atoms and the laser field. The two peak visible in Fig. 6 in the spectrum of  $g^{(2)}$  correspond to the Rabi frequencies  $\Omega_1$  and  $\Omega_2$  experienced by the two atoms. The two peaks can be identified easily by increasing the driving-field intensity. The interatomic distance  $r_{12}$  can then be evaluated through the expressions of Eq. (9) for  $\Omega_1$  and  $\Omega_2$ .

Up to this point, we have focused our analysis on a system geometry where both detectors are equidistant to the scattering atom pair and aligned orthogonal to the interatomic distance vector. The two-photon correlation function, however, is also known to exhibit angular correlation effects for different detector positions [29]. Results for the intensity-intensity correlation function for several detection setups are shown in Fig. 12. It can be seen that the shape of the correlation function does change with the detection geometry. For example, in Fig. 12(b), curves (i), (ii), and (iv) tend to 1 for  $\tau \rightarrow 0$ , whereas curves (iii) and (iv) tend to 0 in this limit. The corresponding power spectra are shown in Fig. 13. From this figure it is apparent that the observables crucial to our distance analysis, namely, the positions of the different peaks

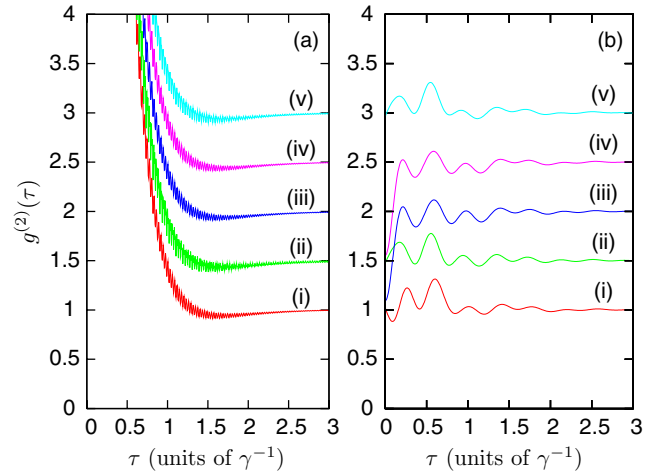


FIG. 12. (Color online) Dependence of the intensity-intensity correlation function on the geometrical setup of the detectors. (a) corresponds to the small-distance case, with parameters as in Fig. 2(a), whereas (b) shows the large-distance case as in Fig. 2(d). The respective curves in the subfigures correspond to different detector setups: (i)  $\theta_1 = \pi/2, \theta_2 = \pi/2$ , (ii)  $\theta_1 = 0, \theta_2 = 0$ , (iii)  $\theta_1 = \pi/2, \theta_2 = 0$ , (iv)  $\theta_1 = \pi/2, \theta_2 = \pi/4$ , (v)  $\theta_1 = \pi/4, \theta_2 = \pi/4$ . Here,  $\theta_i$  ( $i \in \{1, 2\}$ ) are the angles between the interatomic distance vector  $\mathbf{r}_{12}$  and the observation directions  $\mathbf{R}_i$  of the two detectors. Note that the curves have been shifted by integer multiples of 0.5 in the y direction in order to allow for a comparison. Without this artificial shift, all curves roughly coincide with the respective curves (i), but with different high-frequency modulation structure in (a), and different values for  $\tau \rightarrow 0$  in (b).

in the power spectrum, are hardly affected by the detector setup. This can intuitively be understood from our analysis of the peak structure in Fig. 5. There we found that the peak positions depend on characteristic frequencies determined by the internal dynamics of the two-atom system, which is independent of the external detector geometry. Thus, one can expect the peak positions to be unaffected by the detection

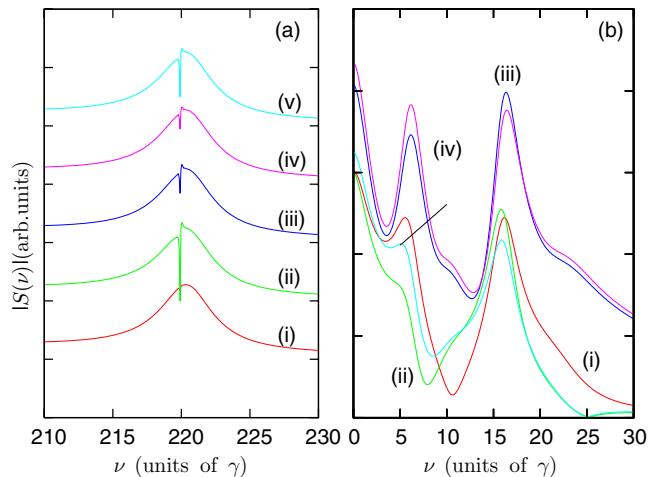


FIG. 13. (Color online) Power spectra of the intensity-intensity correlation functions shown in Fig. 12. In (a), the curves have been shifted by integer multiples of 0.5 in the y direction in order to allow for a comparison. In (b), no additional shift has been applied.

system, whereas the peak amplitudes are subject to amplification or attenuation due to spatial interference effects. For example, in Fig. 13(b), the amplitude of the left peak at around  $\nu=6\gamma$  strongly depends on the detection geometry, further supported by an overall attenuation of the power spectrum for certain detector positions. From our numerical analysis, we find that the detector positions shown in Fig. 1 and used throughout our analysis are well suited for the whole range of considered distances.

The limitations of remote measurement schemes for very small distances have been discussed in our previous work [17]. Fundamental constraints arise from quantum or thermal uncertainties in the position of the particles. Note, however, that for harmonic oscillations of the particles around their equilibrium positions, the classical turning points of the motion can be measured via the optical far-field properties. These again allow one to determine the mean interatomic distance [17]. Further, such schemes are typically limited to distances for which the dipole-dipole interaction energy does not exceed the atomic transition frequencies, namely,  $\Omega_{12} \ll \omega_0$ . From Eq. (8),  $r_{12} = \lambda / (2\pi) (3/2)^{1/3} (\gamma / \Omega_{12})^{1/3}$ . In the optical region, we typically have  $\omega_0 \sim 10^{15}$  Hz,  $\gamma \sim 10^7$  Hz. Then the dipole-dipole interaction energy  $\Omega_{12} \leq 10^{13}$  Hz, and consequently, we obtain a distance measurement limit of  $\lambda/550$ .

#### IV. SUMMARY

In summary, we discussed the properties of the intensity-intensity correlation function of the fluorescence field emitted by two nearby atoms placed inside a standing-wave laser field. In particular, we showed how interatomic distance information can be obtained by analyzing the power spectrum of the correlation function. Our scheme allows us to measure interatomic distances from the classical refraction limit  $\lambda/2$  down to about  $\lambda/550$  using detectors with state-of-the-art time resolution. For a typical optical wavelength, the range is thus from several hundred nanometers to a few nanometers.

#### ACKNOWLEDGMENTS

We would like to thank Han Xiong and Yaping Yang for useful discussions. This research is supported by the Air Force Office of Scientific Research, DARPA-QuIST, and the Office of Naval Research.

#### APPENDIX

The nonvanishing elements of vector  $\mathbf{I}$  are  $\mathbf{I}_1 = i\beta_1^*/2$ ,  $\mathbf{I}_2 = -i\beta_1/2$ ,  $\mathbf{I}_3 = i\beta_2^*/2$ ,  $\mathbf{I}_4 = -i\beta_2/2$ . The nonvanishing elements of matrix  $\mathbf{M}$  are as follows:

$$\mathbf{M}_{(1,1)} = -(1 + i\Delta), \quad \mathbf{M}_{(1,3)} = -(a - ib),$$

$$\mathbf{M}_{(1,5)} = -i\beta_1^*, \quad \mathbf{M}_{(1,12)} = 2(a - ib),$$

$$\mathbf{M}_{(2,2)} = -(1 - i\Delta), \quad \mathbf{M}_{(2,4)} = -(a + ib),$$

$$\mathbf{M}_{(2,5)} = i\beta_1, \quad \mathbf{M}_{(2,11)} = 2(a + ib),$$

$$\mathbf{M}_{(3,1)} = -(a - ib), \quad \mathbf{M}_{(3,3)} = -(1 + i\Delta),$$

$$\mathbf{M}_{(3,6)} = -i\beta_2^*, \quad \mathbf{M}_{(3,14)} = 2(a - ib),$$

$$\mathbf{M}_{(4,2)} = -(a + ib), \quad \mathbf{M}_{(4,4)} = -(1 - i\Delta),$$

$$\mathbf{M}_{(4,6)} = i\beta_2, \quad \mathbf{M}_{(4,13)} = 2(a + ib),$$

$$\mathbf{M}_{(5,1)} = -i\beta_1/2, \quad \mathbf{M}_{(5,2)} = i\beta_1/2,$$

$$\mathbf{M}_{(5,5)} = -2, \quad \mathbf{M}_{(5,7)} = -(a + ib),$$

$$\mathbf{M}_{(5,8)} = -(a - ib), \quad \mathbf{M}_{(6,3)} = -i\beta_2/2,$$

$$\mathbf{M}_{(6,4)} = i\beta_2^*/2, \quad \mathbf{M}_{(6,6)} = -2,$$

$$\mathbf{M}_{(6,7)} = -(a - ib), \quad \mathbf{M}_{(6,8)} = -(a + ib),$$

$$\mathbf{M}_{(7,1)} = -i\beta_2/2, \quad \mathbf{M}_{(7,4)} = i\beta_1^*/2,$$

$$\mathbf{M}_{(7,5)} = -(a + ib), \quad \mathbf{M}_{(7,6)} = -(a - ib),$$

$$\mathbf{M}_{(7,7)} = -2, \quad \mathbf{M}_{(7,11)} = -i\beta_1^*,$$

$$\mathbf{M}_{(7,14)} = i\beta_2, \quad \mathbf{M}_{(7,15)} = 4a,$$

$$\mathbf{M}_{(8,2)} = i\beta_2^*/2, \quad \mathbf{M}_{(8,3)} = -i\beta_1/2,$$

$$\mathbf{M}_{(8,5)} = -(a - ib), \quad \mathbf{M}_{(8,6)} = -(a + ib),$$

$$\mathbf{M}_{(8,8)} = -2, \quad \mathbf{M}_{(8,12)} = i\beta_1,$$

$$\mathbf{M}_{(8,13)} = -i\beta_2^*, \quad \mathbf{M}_{(8,15)} = 4a,$$

$$\mathbf{M}_{(9,1)} = i\beta_2^*/2, \quad \mathbf{M}_{(9,3)} = i\beta_1^*/2,$$

$$\mathbf{M}_{(9,9)} = -2(1 + i\Delta), \quad \mathbf{M}_{(9,12)} = -i\beta_1^*,$$

$$\mathbf{M}_{(9,14)} = -i\beta_2^*, \quad \mathbf{M}_{(10,2)} = -i\beta_2/2,$$

$$\mathbf{M}_{(10,4)} = -i\beta_1/2, \quad \mathbf{M}_{(10,10)} = -2(1 - i\Delta),$$

$$\mathbf{M}_{(10,11)} = i\beta_1, \quad \mathbf{M}_{(10,13)} = i\beta_2,$$

$$\mathbf{M}_{(11,5)} = -i\beta_2/2, \quad \mathbf{M}_{(11,7)} = -i\beta_1/2,$$

$$\mathbf{M}_{(11,10)} = i\beta_1^*/2, \quad \mathbf{M}_{(11,11)} = -(3 - i\Delta),$$

$$\mathbf{M}_{(11,13)} = -(a - ib), \quad \mathbf{M}_{(11,14)} = i\beta_2,$$

$$\mathbf{M}_{(12,5)} = i\beta_2^*/2, \quad \mathbf{M}_{(12,8)} = i\beta_1^*/2,$$

$$\mathbf{M}_{(12,9)} = -i\beta_1^*/2, \quad \mathbf{M}_{(12,12)} = -(3+i\Delta),$$

$$\mathbf{M}_{(12,,14)} = -(a+ib), \quad \mathbf{M}_{(12,15)} = -i\beta_2^*,$$

$$\mathbf{M}_{(13,6)} = -i\beta_1/2, \quad \mathbf{M}_{(13,8)} = -i\beta_2/2,$$

$$\mathbf{M}_{(13,10)} = i\beta_2^*/2, \quad \mathbf{M}_{(13,11)} = -(a-ib),$$

$$\mathbf{M}_{(13,13)} = -(3-i\Delta), \quad \mathbf{M}_{(13,15)} = i\beta_1,$$

$$\mathbf{M}_{(14,6)} = i\beta_1^*/2, \quad \mathbf{M}_{(14,7)} = i\beta_2^*/2,$$

$$\mathbf{M}_{(14,9)} = -i\beta_2/2, \quad \mathbf{M}_{(14,12)} = -(a+ib),$$

$$\mathbf{M}_{(14,14)} = -(3+i\Delta), \quad \mathbf{M}_{(14,15)} = -i\beta_1^*,$$

$$\mathbf{M}_{(15,11)} = i\beta_2/2, \quad \mathbf{M}_{(15,12)} = -i\beta_2/2,$$

$$\mathbf{M}_{(15,13)} = i\beta_1^*/2, \quad \mathbf{M}_{(15,14)} = -i\beta_1/2,$$

$$\mathbf{M}_{(15,15)} = -4.$$

- 
- [1] M. Minsky, U.S. Patent No. 3013467 (1957).  
[2] S. W. Hell, *Nat. Biotechnol.* **21**, 1347 (2003).  
[3] U. W. Rathe and M. O. Scully, *Lett. Math. Phys.* **34**, 297 (1995); A. N. Boto, P. Kok, D. S. Abrams, S. L. Braunstein, C. P. Williams, and J.P. Dowling, *Phys. Rev. Lett.* **85**, 2733 (2000); M. D'Angelo, M. V. Chekhova, and Y. Shih, *ibid.* **87**, 013602 (2001).  
[4] M. O. Scully and K. Drühl, *Phys. Rev. A* **25**, 2208 (1982); M. O. Scully and C. H. Raymond Ooi, *J. Opt. B: Quantum Semiclassical Opt.* **6**, S816 (2004); A. Muthukrishnan, M. O. Scully, and M. S. Zubairy, *ibid.* **6**, S575 (2004).  
[5] W. Denk, J. H. Strickler, and W. W. Webb, *Science* **248**, 73 (1990).  
[6] A. Lewis, M. Isaacson, A. Harootunian, and A. Muray, *Ultramicroscopy* **13**, 227 (1984); A. Lewis, H. Taha, A. Strinkovskii, A. Manevitch, A. Khatchatourians, R. Dekhter, and E. Ammann, *Nat. Biotechnol.* **21**, 1378 (2003).  
[7] G. S. Agarwal, A. C. Brown, L. M. Narducci, and G. Vetri, *Phys. Rev. A* **15**, 1613 (1977).  
[8] A. S. Jahangir Amin and J. G. Cordes, *Phys. Rev. A* **18**, 1298 (1978).  
[9] G. Lenz and P. Meystre, *Phys. Rev. A* **48**, 3365 (1993).  
[10] T. Richter, *Opt. Acta* **30**, 1769 (1983).  
[11] H. S. Freedhoff, *Phys. Rev. A* **19**, 1132 (1979); R. D. Griffin and S. M. Harris, *ibid.* **25**, 1528 (1982).  
[12] Z. Ficek, R. Tanaś, and S. Kielich, *Opt. Acta* **30**, 713 (1983).  
[13] Z. Ficek and R. Tanaś, *Phys. Rep.* **372**, 369 (2002).  
[14] M. Macovei and C. H. Keitel, *Phys. Rev. Lett.* **91**, 123601 (2003).  
[15] E. Betzig, *Opt. Lett.* **20**, 237 (1995).  
[16] C. Hettich, C. Schmitt, J. Zitzmann, S. Kuhn, I. Gerhardt, and V. Sandoghdar, *Science* **298**, 385 (2002).  
[17] J.-T. Chang, J. Evers, M. O. Scully, and M. S. Zubairy, *Phys. Rev. A* **73**, 031803(R) (2006).  
[18] T. Azim, M. Ikram, and M. S. Zubairy, *J. Opt. B: Quantum Semiclassical Opt.* **6**, 248 (2004); F. Ghafoor, S. Qamar, and M. S. Zubairy, *Phys. Rev. A* **65**, 043819 (2002); S. Qamar, S.-Y. Zhu, and M. S. Zubairy, *ibid.* **61**, 063806 (2000); F. Le Kien, G. Rempe, W. P. Schleich, and M. S. Zubairy, *ibid.* **56**, 2972 (1997); M. Sahrai, H. Tajalli, K. T. Kapale, and M. S. Zubairy, *ibid.* **72**, 013820 (2005).  
[19] G. C. Hegerfeldt and D. Seidel, *J. Opt. B: Quantum Semiclassical Opt.* **4**, 245 (2002).  
[20] C. Skornia, J. von Zanthier, G. S. Agarwal, E. Werner, and H. Walther, *Phys. Rev. A* **64**, 063801 (2001).  
[21] M. O. Scully and C. H. Raymond Ooi, *J. Opt. B: Quantum Semiclassical Opt.* **6**, S575 (2004).  
[22] T. G. Rudolph, Z. Ficek, and B. J. Dalton, *Phys. Rev. A* **52**, 636 (1995); J. G. Cordes and W. Roberts, *ibid.* **29**, 3437 (1984).  
[23] Z. Ficek and S. Swain, *Quantum Interference and Coherence: Theory and Experiments* (Springer, Berlin, 2005).  
[24] R. H. Lehberg, *Phys. Rev. A* **2**, 883 (1970).  
[25] G. S. Agarwal, in *Quantum Optics*, edited by G. Hohler, Springer Tracts in Modern Physics, Vol. 70 (Springer, Berlin, 1974).  
[26] J. Evers, M. Kiffner, M. Macovei, and C. H. Keitel, *Phys. Rev. A* **73**, 023804 (2006).  
[27] M. O. Scully and M. S. Zubairy, *Quantum Optics* (Cambridge University Press, Cambridge, UK, 1997).  
[28] P. W. Milonni and P. L. Knight, *Phys. Rev. A* **10**, 1096 (1974).  
[29] H. Steudel and Th. Richter, *Ann. Phys.* **35**, 122 (1978); Th. Richter, *ibid.* **36**, 266 (1979); *Opt. Commun.* **80**, 285 (1991).